Journal of Materials Science & Technology 126 (2022) 203–214

Contents lists available at ScienceDirect

Journal of Materials Science & Technology

journal homepage: www.elsevier.com/locate/jmst

Research Article

Pressureless two-step sintering of ultrafine-grained refractory metals: Tungsten-rhenium and molybdenum

Zhongyou Que[a,1], Zichen Wei[a,1], Xingyu Li[a], Lin Zhang[a,*], Yanhao Dong[b,*], Mingli Qin[a], Junjun Yang[a], Xuanhui Qu[a], Ju Li[b,c,*]

[a] Beijing Advanced Innovation Center for Materials Genome Engineering, Institute for Advanced Materials and Technology, University of Science and Technology Beijing, Beijing 100083, China
[b] Department of Nuclear Science and Engineering, Massachusetts Institute of Technology, Cambridge, MA 02139, USA
[c] Department of Materials Science and Engineering, Massachusetts Institute of Technology, Cambridge, MA 02139, USA

ARTICLE INFO

Article history:
Received 12 December 2021
Revised 21 January 2022
Accepted 23 January 2022
Available online 8 April 2022

Keywords:
Powder metallurgy
Refractory metals
Porosity
Two-step sintering
Grain growth

ABSTRACT

The challenge of sintering ultrafine-grained refractory metals and alloys to full density is hereby addressed by pressureless two-step sintering in tungsten-rhenium alloy and pure molybdenum. Using properly processed nano powders (~50 nm average particle size), we are able to sinter W-10Re alloy to 98.4% density below 1200 °C while maintaining a fine grain size of 260 nm, and sinter molybdenum to 98.3% density below 1120 °C while maintaining a fine grain size of 290 nm. Compared to normal sintering, two-step sintering offers record-fine grain sizes and better microstructural uniformity, which translates to better mechanical properties with higher hardness (6.3 GPa for tungsten-rhenium and 4.0 GPa for molybdenum, both being the highest in all pressurelessly sintered samples of the respective material system) and larger Weibull modulus. Together with our previous demonstration in tungsten, we believe that two-step sintering is a general effective method to produce high-quality fine-grained refractory metals and alloys, and the lessons learned here are transferable to other materials for powder metallurgy.

1. Introduction

Pressureless sintering of fine-grained refractory metals and alloys to full density is a challenging powder-metallurgy problem and it is of great interest to many technologies, including aerospace, fusion energy, microelectronics, and other high-temperature/extreme-environment applications [1,2]. This challenge has recently been addressed by us in pure tungsten (W) using two-step sintering [3,4]. Starting with ~50 nm nano powders, we were able to pressurelessly sinter high-purity W to a relative density ρ=99.3% and an average grain size G_{avg}=290 nm, at ~1200 °C (~0.4 of the melting point T_m=3422 °C=3695 K for W) in flowing H_2. The success of two-step sintering in processing dense ultrafine-grained W is encouraging and we expect similar practices to be applicable to other refractory metals and alloys. Here we report successful two-step sintering of tungsten-rhenium (W-Re) alloy and pure molybdenum (Mo), where ρ≈99% and G_{avg}≈300 nm can be achieved in both systems. To the end, with further modified nano powders, we are optimistic about producing dense nanocrystalline refractory metals and alloys via pressureless sintering technique in the future.

W-Re alloys have a high melting point, high elastic modulus, high density, and high thermal conductivity, so they are widely used in aerospace, thermocouple, and electronics industries [5–8]. Compared to pure W, the addition of Re increases the room-temperature ductility, the recrystallization temperature, and the ultimate tensile strength, and decreases the ductile-brittle transition temperature (often termed as the rhenium effect) [9–12]. The alloying element Re is also reported to decrease the thermodynamic driving force for grain coarsening, and thus helps to inhibit grain growth during the sintering process [13,14]. For sintered products, refining and homogenizing the microstructure is critical to many application-oriented properties, including solving the brittle issue of W alloys [15–20]. In addition, W-Re alloys are widely used as high-temperature thermocouples (up to 1500-3000 °C). The long-time high-temperature service indicates stable microstructure and sluggish diffusion kinetics of W-Re alloys. Indeed, despite a lowered melting temperature (T_m≈3200 °C=3473 K for W-10Re), Re addition increases the recrystallization temperature of W-Re al-

* Corresponding authors.
E-mail addresses: zlin@ustb.edu.cn (L. Zhang), dongyh@mit.edu (Y. Dong), liju@mit.edu (J. Li).
[1] These two authors contribute equally.

https://doi.org/10.1016/j.jmst.2022.01.033
1005-0302/

loys to >1500 °C for 90 wt% W-10 wt% Re (W-10Re) compared to 1100-1200 °C for W [21]. How the suppressed recrystallization kinetics correlates with grain boundary diffusion and affects sintering kinetics is unclear. On the processing side, W-Re alloys are commonly produced through the powder metallurgy route, where powder compacts are firstly partially densified by pressureless sintering at high temperatures (~2000 °C) and then go through further densification steps by hot isostatic pressing or plastic deformation [15,22]. Special sintering techniques such as spark plasma sintering are also used for one-step, direct densification, albeit with limited geometry and sample size [14,23]. In comparison, there are few reports for successful pressureless sintering of W-Re alloys to full density. For example, Ivanov et al. [24] pressurelessly sintered blended 75 wt% W-25 wt% Re (W-25Re) powders to obtain ρ=93.1% and G_{avg}≈45 μm and mechanically alloyed nanocrystalline W-25Re powders to obtain ρ=92.6% and G_{avg}=25 μm at 2350 °C for 3 h; Lai et al. [25] pressurelessly sintered W-25Re powders (with secondary particle morphology produced by spray drying and fine primary particle size) to obtain ρ=93% and G_{avg}≈3 μm at 1900 °C for 0.5 h.

Molybdenum is widely used in high-tech fields including sputtering targets and electronic devices due to its high stability, high creep resistance and high thermal conductivity [26–30]. Mo is also mainly processed through powder metallurgy route. High density, fine grain size, and uniform microstructure help to improve the performance of Mo products, especially for sputtering targets. Conventionally, Mo powders are sintered at 2000-2400°C to reach ρ=90%-95% [31]. Its grain size is very difficult to control due to high temperature and the lack of second-phase pinning. Regarding the sintering of fine-grained Mo samples, previous attempts in the literature mostly ended up with coarse grain structure and there were few reports on dense ultrafine-grained Mo, even when nano powders were used. For example, Kim et al. [32] pressurelessly sintered Mo nano powders at 1200 °C for 1 h to obtain ρ=95% and G_{avg}=1.4 μm; Hu et al. [33] pressurelessly sintered ~30 nm Mo nano powders at 1500 °C without holding to obtain ρ=99.1% and G_{avg}=7 μm or at 1200 °C for 1 h to obtain ρ=93.5% and G_{avg}=1.7 μm.

With the above backgrounds, it would be valuable to investigate and fill in the knowledge of low-temperature pressureless sintering of W-Re alloys and pure Mo, especially with high sintered density, fine grain size and uniform microstructure that would benefit properties and any follow-up processing. In the following, we report the sintering kinetics of W-10Re and Mo nano powders, which are similarly synthesized and processed to the W nano powders used in our previous work. We shall demonstrate successful pressureless two-step sintering of W-10Re and Mo close to full density below 1300 °C. For W-10Re, the best practice gives ρ=98.4%, G_{avg}=270 nm (5.4-fold coarsening from ~50 nm starting powders), and a hardness of 6.3 GPa that is the highest in all pressureless sintered W-Re alloys. For Mo, the best practice gives ρ=98.3%, G_{avg}=290 nm (5.8-fold coarsening from ~50 nm starting powders), and a hardness of 4.0 GPa that is the highest in all pressureless sintered Mo. Inferred grain-boundary diffusivity data and key parameters for two-step sintering are discussed and compared with our previous results in pure W without alloying, which offers guidance to produce better refractory metals and their alloys including for near-net-shape processing and in their particle-strengthened forms (e.g., with oxides or carbides).

2. Experimental procedures

Nano-sized W-10Re and Mo powders were prepared by solution combustion and H_2 reduction method similar to our previous work on W, using $(NH_4)_6H_2W_{12}O_{40}\bullet xH_2O$ and NH_4ReO_4 precursors with W:Re=9:1 weight ratio for W-10Re and $H_{24}Mo_7N_6O_{24}\bullet 4H_2O$ precursor for Mo [34,35]. The synthesized W-10Re and Mo nano powders were either directly used (abbreviated as “raw powders” hereafter) or centrifuge-sieved in anhydrous ethanol at 3000 r/min to remove the large particles (abbreviated as “sieved powders” hereafter). To prepare green bodies, the powders were uniaxially pressed into pellets (diameter: 10 mm, thickness: ~1 mm) under 750 MPa at room temperature. Two different kinds of sintering experiments were conducted on green compacts in a flowing H_2 atmosphere (high purity, flow rate: 0.6 L/min). (i) Constant-heating-rate sintering experiments by heating the green bodies to a preset temperature (900 °C to 1500 °C) under 5 °C/min without holding, followed by immediate cooling under 10 °C/min down to room temperature. These experiments were used to study the sintering kinetics and the proper conditions for two-step sintering. (ii) Two-step sintering experiments by firstly heating the green compacts under 5 °C/min to a higher first-step temperature T_1 without holding (or with 0.5 h holding), then cooling down to a lower second-step temperature T_2 and holding for 10 h, and lastly cooling under 10 °C/min down to room temperature.

The powders were inspected under a scanning electron microscope (SEM; Hitachi UHR SU8100) and their size distributions were measured manually over 300 particles. Densities of the sintered samples were measured by Archimedes' method. We used a theoretical density of 19.4 g/cm^3 for W-10Re [36,37] and 10.2 g/cm^3 for Mo [38] to calculate the relative density ρ. Sintering rates in constant-heating-rate sintering experiments were calculated from the slopes between each data point and its two neighboring data points (or one neighboring data point for the first/last data point) in the ρ-time plot (temperature was converted to time by the heating rate). Fractured surfaces of sintered samples were inspected under SEM, which showed intergranular fracture for all the samples. Average grain size G_{avg} of sintered samples was calculated from measurements over 300 grains. Electron backscatter diffraction (EBSD; using diffractometer HKL Channel 5 on a Zeiss Ultra 55 field emission SEM) measurements were conducted on polished surfaces (first by mechanically polishing and then by electropolishing in NaOH solution) of sintered samples. Vickers hardness H was measured on polished surfaces of sintered samples using a Vickers diamond pyramid indenter under 200 gf (1.96 N) load and with 15 s duration. Distances between neighboring indents were set to larger than 500 μm. Weibull modulus m of H was calculated by

$$p(H) = 1 - \exp\left[-\left(\frac{H}{H_0}\right)^m\right] \quad (1)$$

where H_0 is characteristic hardness. To linearize skewed Weibull data, probability $p(H)$ is defined as

$$p(H) = \frac{(i-0.3)}{(n+0.4)} \quad (2)$$

where i is the rank of the harness data and n is the total number of hardness measurements (n is 33 for W-10Re and 25 for Mo) [39].

3. Results

3.1. Powders

Fig. 1(a) shows the fine particle sizes (average particle size: 53 nm) of the as-synthesized raw W-10Re powders. But they contain many large particles, which broaden the size distribution and constitute a large volume fraction (see accumulative volume fraction as a function of particle sizes in Fig. 1(c)). These observations apply to the as-synthesized raw Mo powders (Fig. 1(d) and (f), average particle size: 67 nm) and are similar to what we noted for W nano powders (synthesized by the same combustion-reduction method) in our previous work [4]. Such powder characteristics often lead

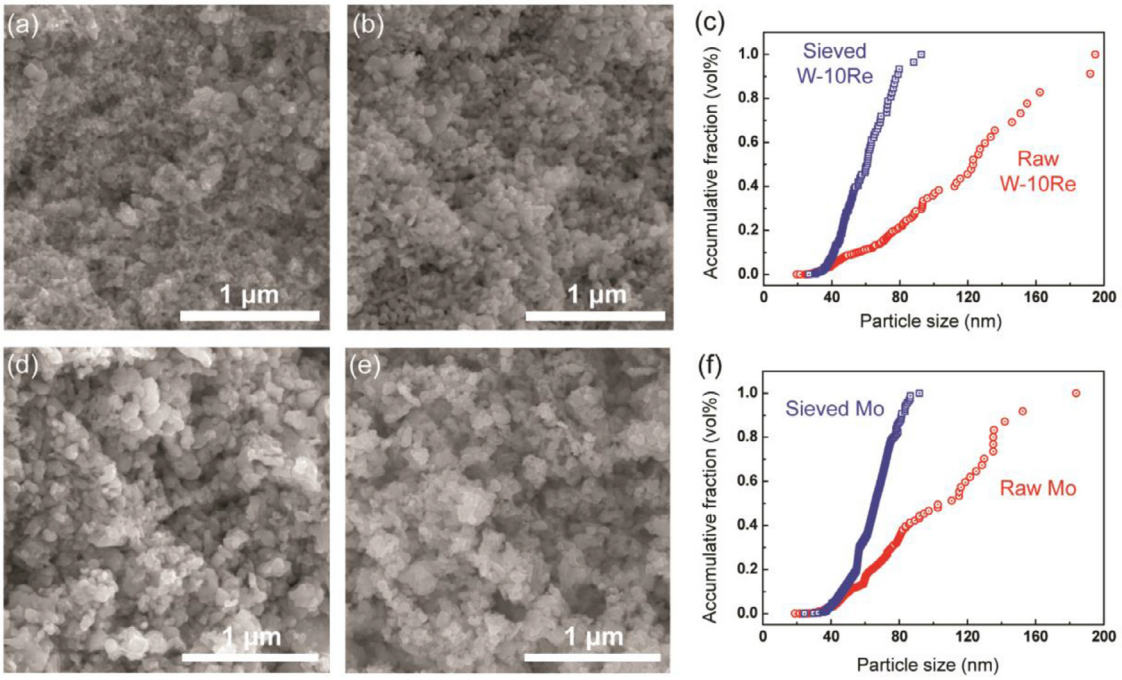

Fig. 1. SEM images showing the morphology of (a) the raw and (b) sieved W-10Re powders, and (c) W-10Re powders' particle size distributions, and SEM images of (d) the raw and (e) sieved Mo powders, and (f) Mo powders' particle size distributions. Note *y* axis in (c) and (f) shows the accumulative volume fraction in the unit of vol%.

to heterogeneous densification, localized grain growth, and sample distortions, which are detrimental to sintering, especially for removing the last few percentages of residue pores in the final stage. To remove the large particles and narrow down the particle size distribution, the as-synthesized W-10Re and Mo powders were centrifuge-sieved (Fig. 1(b) for W-10Re and Fig. 1(e) for Mo). The sieved powders have slightly smaller average particle sizes (48 nm for sieved W-10Re and 55 nm for sieved Mo) and narrower size distributions than the raw powders, and no longer contain >100 nm particles.

3.2. Sintering kinetics

To study the sintering kinetics, constant-heating-rate sintering experiments (details described in Section 2) were conducted. The microstructures of W-10Re samples sintered at different temperatures (without holding) are shown in Fig. 2 and Fig. S1 in Supplementary Information. Uniform microstructures were observed throughout the sintering, for both the raw-powder (Fig. 2(a-c)) and sieved-powder derived W-10Re samples (Fig. 2(d-f)). This is different from our previous observations in W [4], which has bimodal particle/grain size distributions and less uniform microstructures below 1200 °C, especially for the raw-powder derived samples. It could be due to Re alloying that decreases the anisotropy in surface/grain boundary energy and mobility or due to better W-10Re powders with narrower size distribution and less large particles. Regarding the sintering, the relative densities of the sieved-powder derived W-10Re samples are slightly lower than those of the raw-powder derived W-10Re samples at ≤1100 °C (ρ<60%) but become much higher than the latter at >1100 °C (Fig. 3(a); detailed sintering data available in Table 1). When sintered at 1500 °C without holding, the sieved-powder derived W-10Re sample has ρ=98.1%, compared to ρ=95.2% for the raw-powder derived W-10Re sample sintered at the same condition. It shows the benefit of powder sieving in improving the intermediate- and final-stage sinterability. For the grain size, the raw-powder and sieved-powder derived W-10Re samples have similar sizes at ≤1300 °C (Fig. 3(b), despite a relative density difference of ~6%). The grain size increases more rapidly above 1300 °C (ρ>85%) and shows a "jump" at 1350 °C, especially for the raw-powder derived sample. The calculated sintering rate dρ/dt (Fig. 3(c)) reaches maximum values at 1150 °C (at ρ=66% for the raw-powder derived W-10Re sample and 71% for the sieved-powder derived W-10Re sample). The peak sintering rate is higher for the sieved-powder derived W-10Re samples.

Table 1
Sintering data of W-10Re from constant-heat-rate sintering and two-step sintering.

Sintering conditions	Raw powders		Sieved powders	
	ρ (%)	G_{avg} (nm)	ρ (%)	G_{avg} (nm)
900 °C for 0 h	54	98	54	73
1000 °C for 0 h	56	120	55	82
1050 °C for 0 h	59	150	57	95
1100 °C for 0 h	61	180	59	120
1150 °C for 0 h	66	190	71	160
1200 °C for 0 h	72	230	78	210
1250 °C for 0 h	77	300	84	310
1300 °C for 0 h	82	350	88	340
1350 °C for 0 h	85	680	93	510
1400 °C for 0 h	92	750	95.0	560
1500 °C for 0 h	95.2	1290	98.1	1160
1200 °C for 0 h, 1100 °C for 10 h	80	250	82	240
1200 °C for 0 h, 1150 °C for 10 h	92	300	98.4	260
1230 °C for 0 h, 1150 °C for 10 h	94	350	98.6	310
1250 °C for 0 h, 1150 °C for 10 h	97.4	470	99.6	400
1300 °C for 0 h, 1200 °C for 10 h	99.0	550	99.5	530

The microstructures of Mo samples sintered at different temperatures (without holding) are shown in Fig. 4 and Fig. S2 in Supplementary Information. Uniform microstructures were again observed throughout the sintering, for both the raw-powder (Fig. 4(a-c)) and sieved-powder derived Mo samples (Fig. 4(d-f)). A much larger grain size was observed for the raw-powder derived Mo sample sintered at 1300 °C (Fig. 4(c)) than the sieved powder derived one (Fig. 4(f)). Regarding the sintering, the relative densities of the sieved-powder derived Mo samples are slightly lower than those of the raw-powder derived Mo samples at ≤1150 °C

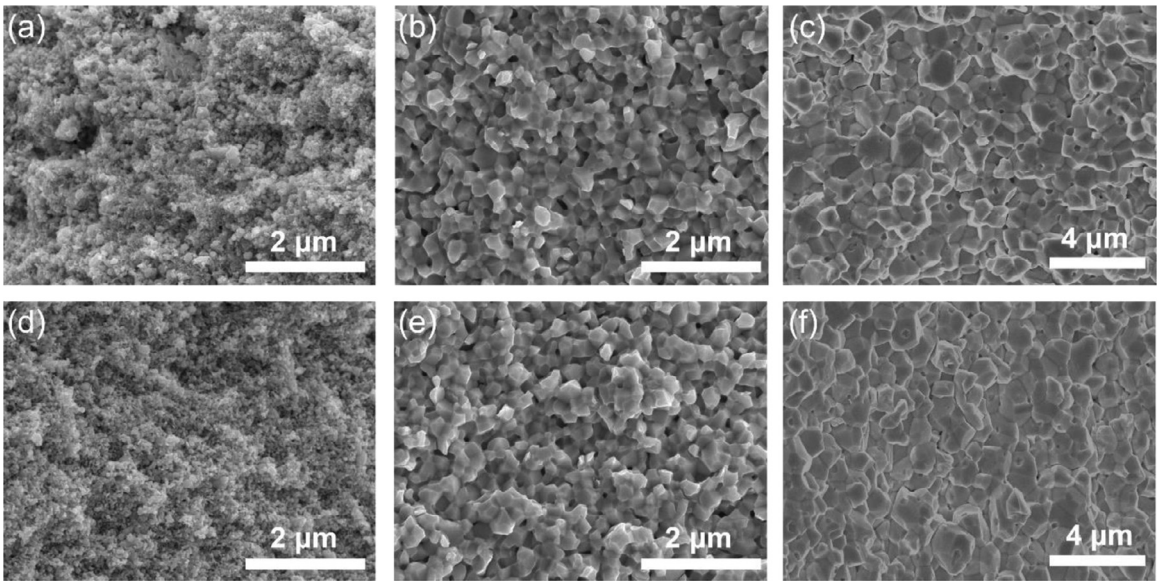

Fig. 2. Microstructures (fracture surfaces) of the raw-powder derived W-10Re samples sintered at (a) 900 °C, (b) 1300 °C, and (c) 1500 °C without holding, and the sieved-powder derived W-10Re samples sintered at (d) 900 °C, (e) 1300 °C, and (f) 1500 °C without holding.

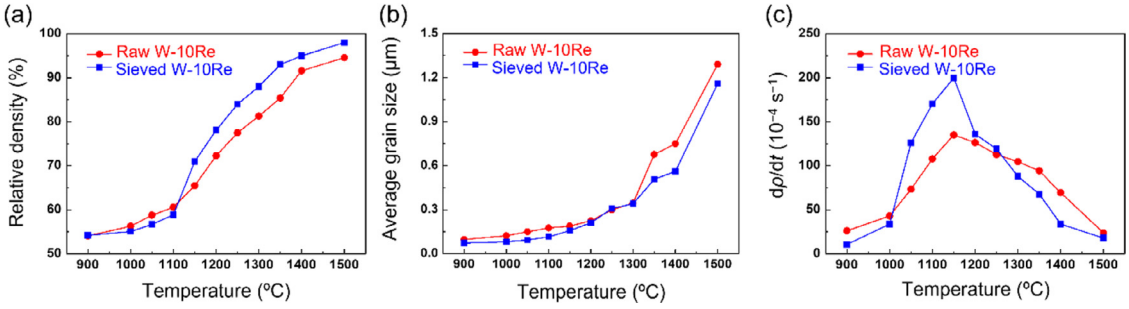

Fig. 3. (a) Relative density, (b) average grain size, and (c) sintering rate dρ/dt of the raw-powder (in red) and sieved-powder (in blue) derived W-10Re samples in constant-sintering-rate experiments up to 1500 °C.

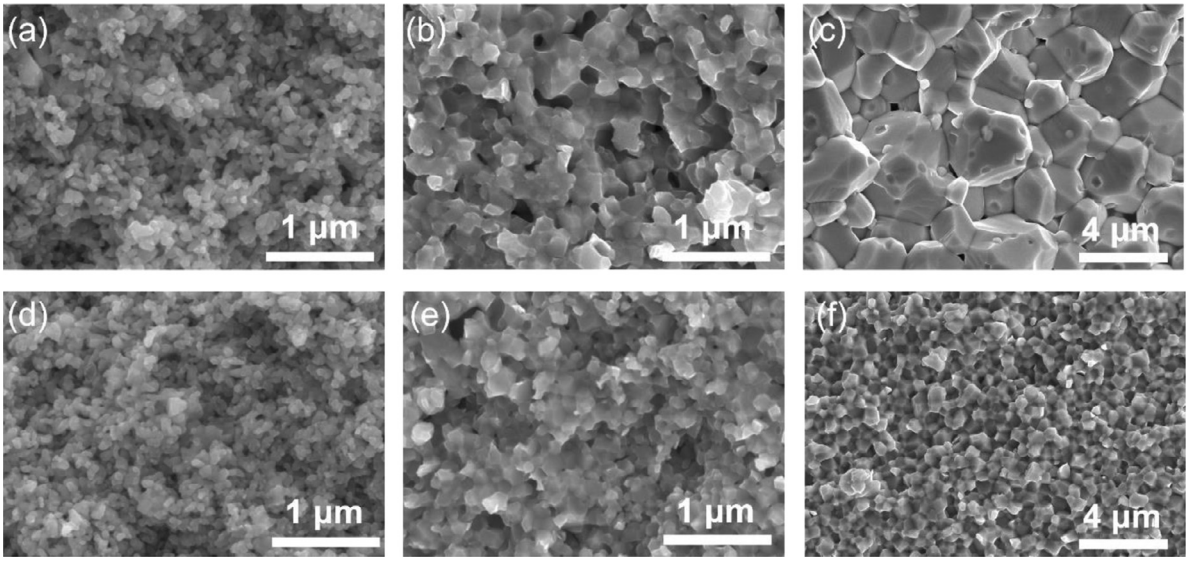

Fig. 4. Microstructures (fracture surfaces) of the raw-powder derived Mo samples sintered at (a) 900 °C, (b) 1100 °C, and (c) 1300 °C without holding, and the sieved-powder derived W-10Re samples sintered at (d) 900 °C, (e) 1100 °C, and (f) 1300 °C without holding.

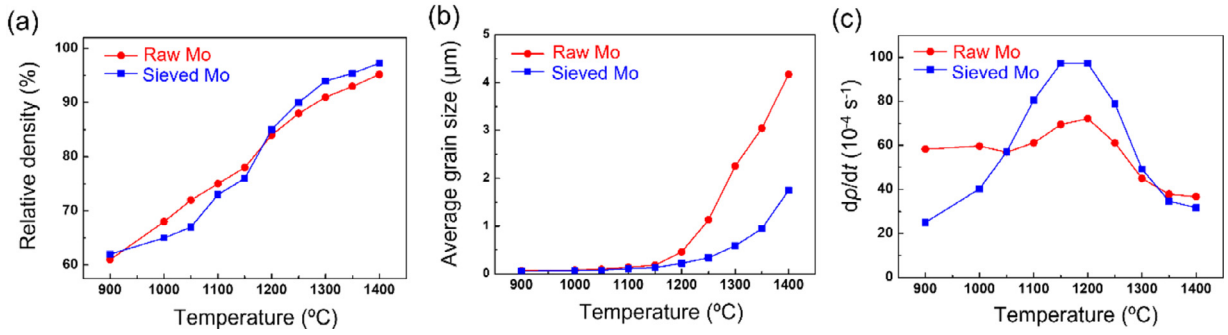

Fig. 5. (a) Relative density, (b) average grain size, and (c) sintering rate $d\rho/dt$ of the raw-powder (in red) and sieved-powder (in blue) derived Mo samples in constant-sintering-rate experiments up to 1400 °C.

(ρ<80%) but become higher than the latter at >1200 °C (Fig. 5(a); detailed sintering data available in Table 2). When being sintered at 1400 °C without holding, the sieved-powder derived Mo sample has ρ=97.3%, compared to ρ=95.2% for the raw-powder derived Mo sample sintered at the same condition. It again shows the benefit of powder sieving in improving the intermediate- and final-stage sinterability. For the grain size, there is limited grain growth for the raw-powder and sieved-powder derived Mo samples at ≤1150 °C (Fig. 5(b)). Rapid grain growth onsets at 1200 °C in the raw-powder derived Mo samples, reaching G_{avg}=4.2 μm at 1400 °C without holding. In contrast, the grain growth in the sieved-powder derived Mo samples is much slower (e.g., reaching G_{avg}=1.7 μm at 1400 °C without holding), despite higher ρ than the raw-powder derived ones under the same sintering condition. The dramatically different grain growth kinetics of the raw and sieved nano powders in constant-heating-rate sintering experiments is only observed in Mo, but not in W or W-10Re. The calculated sintering rate $d\rho/dt$ (Fig. 5(c)) reaches the maximum values at 1150-1200 °C and the sieved-powder derived Mo samples have a higher peak sintering rate than the raw-powder derived ones.

3.3. Grain boundary diffusivity and activation energy

For better quantifications, we calculated the apparent grain boundary diffusivity D_{GB} and its activation energy E_a from the sintering data of the sieved-powder derived samples using the following two models. (Abnormal sintering behaviors due to localized sintering and grain growth were observed in the raw-powder derived W samples in our previous work. The fast grain growth in the raw-powder derived Mo samples may also be due to similar reasons.) We firstly used the model proposed by Johnson [40] and later adapted by Young and Cutler [41]

$$\left(\frac{\Delta L}{L_0}\right)^{2.06}\frac{d(\Delta L/L_0)}{dt}=\frac{11.2\gamma\Omega\delta D_{GB}}{k_B T G_{avg}^4} \quad (3)$$

where L_0 is the initial sample length before sintering, ΔL is the change in sample length during sintering, $\Delta L/L_0$ is the linear shrinkage, t is the time, γ is the grain boundary energy taken as 2.26 J/m^2 for W-10Re and 1.78 J/m^2 for Mo [42], Ω is the atomic volume taken as 1.58 × 10^{-29} m^3 for W-10Re and 1.56 × 10^{-29} m^3 for Mo, δ is the grain boundary thickness taken as 1 nm, k_B is Boltzmann constant, and T is the absolute temperature in K. We also assume an Arrhenius relationship for D_{GB}, namely

$$D_{GB}=D_{GB,0}\exp\left(-\frac{E_a}{k_B T}\right) \quad (4)$$

where $D_{GB,0}$ is the pre-exponent factor. Chosen the data with ρ<90% (here we used the data with ρ in the range of 59%-88% for W-10Re, 65%-88% for Mo, and 58%-85% for W), we compared the calculated D_{GB} of W-10Re and Mo in the present work and W in our previous work as a function of the inverse homologous temperature (T_m/T) in Fig. 6(a). W-10Re and W apparently have similar D_{GB} at the same homologous temperature T/T_m (e.g., ~3.2 × 10^{-18} m^2/s at T/T_m=0.4) and similar E_a (2.5 eV for W-10Re and 2.2 eV for W). In comparison, the diffusivity data of Mo lie at a higher homologous temperature range (lower-left conner of Fig. 6(a)), indicating more sluggish grain boundary diffusion in Mo at the same homologous temperature. Indeed, Mo has larger E_a of 4.3 eV than W-10Re and W.

We next used the sintering model from Herring's general dimensional arguments [43]

$$\frac{d\rho}{\rho dt}=F(\rho)\frac{3\gamma\Omega\delta D_{GB}}{k_B T G_{avg}^4} \quad (5)$$

where $F(\rho)$ is a dimensionless function depending on ρ and taken as 12,000 for ρ between 0.75 and 0.85 [44]. Due to limited data, here we used the sintering data with ρ in the range of 78%-88% for W-10Re, 67%-81% for Mo, and 71%-85% for W and still assumed a constant $F(\rho)$=12,000. The calculated D_{GB} from Herring's method is plotted in Fig. 6(b) against T_m/T, which shows consistent results to Johnson's method: W-10Re and W have similar D_{GB} at the same homologous temperature and similar E_a (2.9 eV for W-10Re and 3.5 eV for W), while Mo has lower D_{GB} and larger E_a (3.9 eV). Lastly, we note the calculated E_a of the sieved-powder derived W-10Re, Mo, and W samples all lie on the lower end of the reported E_a in the corresponding material systems [33,45-49], which indicates the high sinterability of our synthesized nano powders.

3.4. Two-step sintering

With the sieved nano powders, the above constant-heating-rate sintering experiments give 98.1% dense W-10Re with G_{avg}=1.16 μm at 1500 °C without holding and 97.3% dense Mo with G_{avg}=1.75 μm at 1400 °C without holding. Higher densities are also achievable by some constant temperature holding, though at the cost of larger grain sizes. Obviously, to obtain dense ultrafine-grained samples, a different sintering schedule is required. Two-step sintering has a heating schedule that firstly sinters the samples to above 70%-80% relative density at a higher temperature T_1, then cools down to a lower temperature T_2 to reach full density while suppressing the grain growth. It has enabled pressureless sintering of fine-grained materials, including many ceramics and recently shown by us in W [4,50-55]. To apply two-step sintering in W-10Re and Mo, we borrowed the knowledge we learnt in W (the first step sintering at T_1 should reach a critical density ρ_c≈71%). This was achieved by heating the sieved-powder derived W sample to T_1=1230 °C, and the second step sintering at T_2=1180 °C for 10 h gives final density ρ=99.3% and G_{avg}=290 nm [4]. Bearing the similarities between W-10Re and W in mind, we started with the first step sintering at T_1=1150-1250 °C and tried different two-step

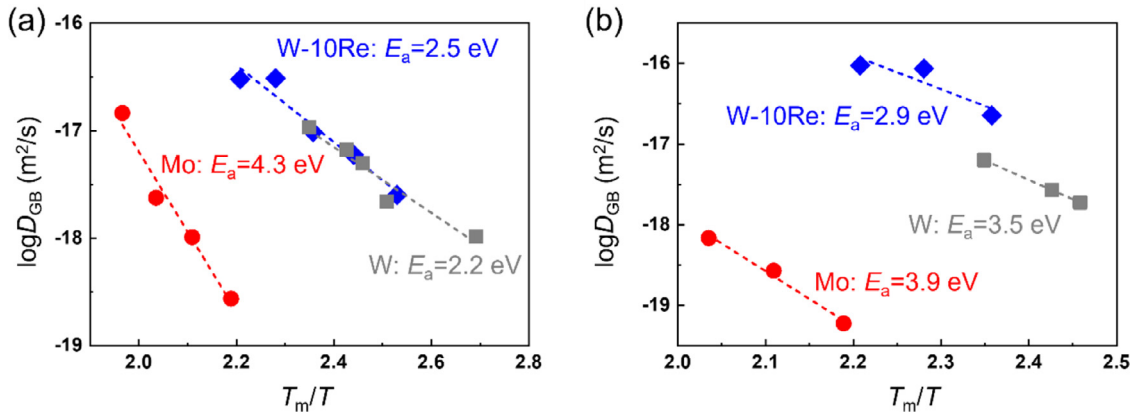

Fig. 6. Arrhenius plot of D_{GB} and calculated E_a using (a) Johnson's method and (b) Herring's method. Dash lines are linear fitting results of the corresponding data points. Linear fitting parameter R^2 is 0.940 for W, 0.950 for W-10Re, and 0.973 for Mo in (a) and 1.000 for W, 0.812 for W-10Re, and 0.987 for Mo in (b).

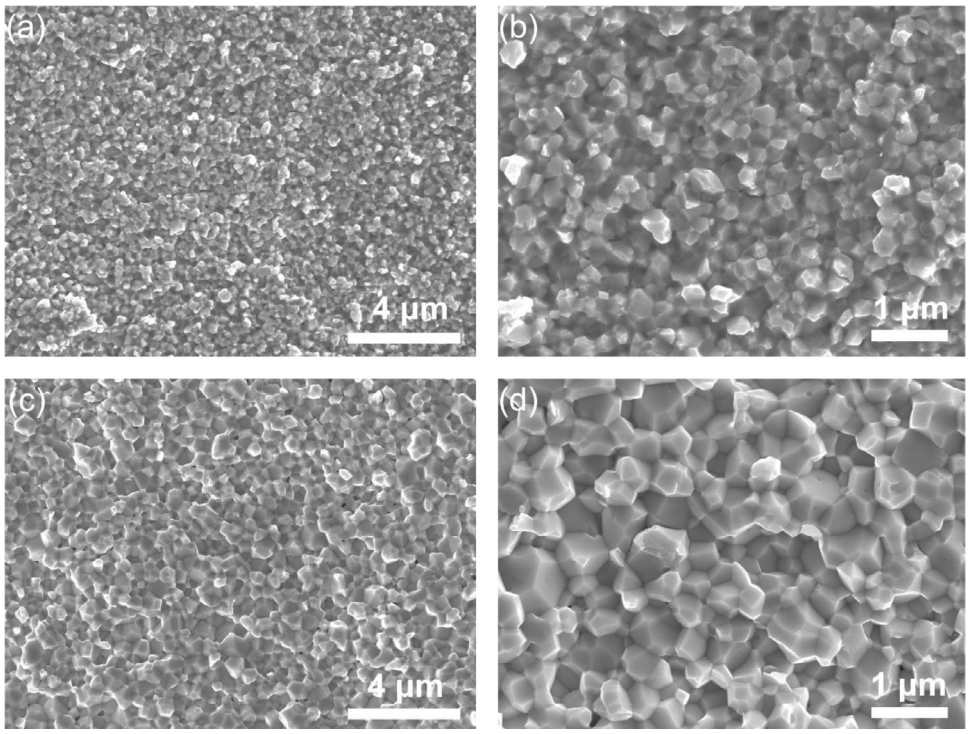

Fig. 7. Fracture surfaces of (a, b) the sieved-powder derived W-10Re sample two-step sintered at T_1=1200 °C for 0 h and T_2=1150 °C for 10 h, and (c, d) the raw-powder derived W-10Re samples two-step sintered at T_1=1300 °C for 0 h and T_2=1200 °C for 10 h.

sintering conditions (Table 1). We found that (i) the sieved-powder derived W-10Re samples always show higher densities and smaller grain sizes than the raw-powder derived W-10Re samples under the same sintering conditions, (ii) a critical density ρ_c≈78% (obtained at T_1=1200 °C, with G_{avg}=210 nm and about 4-fold coarsening from starting powders) is required to enable full densification within 10 h second step sintering at T_2, (iii) the best two-step sintering practice at T_1=1200 °C for 0 h and T_2=1150 °C for 10 h gives ρ=98.4% and G_{avg}=260 nm for the sieved-powder derived W-10Re samples, and (iv) there is still active grain growth in the second step sintering at T_2. The fractured surface of the sieved-powder derived W-10Re sample two-step sintered at T_1=1200 °C for 0 h and T_2=1150 °C for 10 h is shown in Fig. 7(a, b), which is pore-free and has a finer and more uniform microstructure than the raw-powder derived W-10Re sample with a similar density (ρ=99.0%, two-step sintered at T_1=1300 °C for 0 h and T_2=1200 °C for 10 h; Fig. 7(c, d)). Overall, two-step sintering successfully refines the grain size of dense W-10Re samples down to <500 nm.

For Mo that has much lower melting temperature than W, we expected lower absolute first/second sintering temperatures and similar ρ_c, so we tried different two-step sintering conditions with T_1=1100-1150 °C (Table 2). (Here we used a holding time of 0.5 h at T_1 because of early trials, and the sintering data of 0.5 h at T_1 are listed in Table S1 in Supplementary Information.) We mostly focused on the sieved-powder derived Mo samples and found that (i) the sieved-powder derived Mo sample shows higher densities and smaller grain size than the raw-powder derived Mo sample two-step sintered at T_1=1120 °C for 0.5 h and T_2=1070 °C for 10 h, (ii) a critical density ρ_c≈81% (obtained at T_1=1120 °C, with G_{avg}=140 nm and about 3-fold coarsening from starting powders) is required to enable full densification within 10 h second step sintering at T_2, (iii) the best two-step sintering practice at T_1=1120

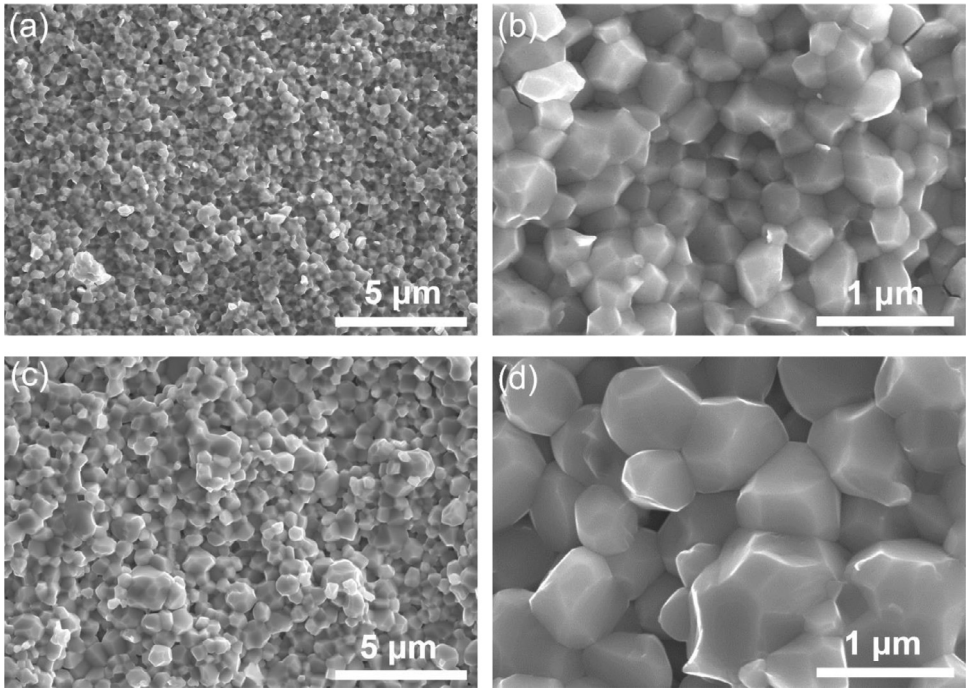

Fig. 8. Fracture surfaces of (a, b) the sieved-powder and (c, d) raw-powder derived Mo samples two-step sintered at T_1=1120 °C for 0.5 h and T_2=1070 °C for 10 h.

Table 2
Sintering data of Mo from constant-heat-rate sintering and two-step sintering.

Sintering conditions	Raw powders		Sieved powders	
	ρ (%)	G_{avg} (nm)	ρ (%)	G_{avg} (nm)
900 °C for 0 h	61	67	62	58
1000 °C for 0 h	68	80	65	68
1050 °C for 0 h	72	96	67	79
1100 °C for 0 h	75	140	73	110
1150 °C for 0 h	78	180	76	130
1200 °C for 0 h	84	460	85	220
1250 °C for 0 h	88	1130	90	340
1300 °C for 0 h	91	2250	94	580
1350 °C for 0 h	93	3050	95.4	950
1400 °C for 0 h	95.2	4170	97.3	1750
1100 °C for 0.5 h, 1050 °C for 10 h	/	/	85	160
1130 °C for 0.5 h, 1030 °C for 10 h	/	/	89	180
1100 °C for 0.5h, 1050 °C for 10 h	/	/	95.2	250
1120 °C for 0.5 h, 1070 °C for 10 h	92	490	98.3	290
1150 °C for 0 h, 1100 °C for 10 h	/	/	98.5	850

°C for 0.5 h and T_2=1070°C for 10 h gives ρ=98.3% and G_{avg}=290 nm for the sieved-powder derived Mo samples, and (iv) there is still active grain growth in the second step sintering at T_2. The fractured surface of the sieved-powder derived Mo sample two-step sintered at T_1=1120 °C for 0.5 h and T_2=1070 °C for 10 h is shown in Fig. 8(a, b), which shows a high density and has a finer and more uniform microstructure than the raw-powder derived Mo sample sintered under the same condition (ρ=92% and G_{avg}=490 nm, Fig. 8(c, d)). Again, two-step sintering successfully refines the grain size of dense Mo samples down to <500 nm.

3.5. Quantification of microstructural uniformity

For better quantifications of the microstructure especially the grain size uniformity, we conducted EBSD measurements on differently sintered W-10Re (Fig. 9) and Mo (Fig. 10) samples. By comparing the inverse pole figure map (Fig. 9(a, e, i), Fig. 10(a, e, i)) and normalized grain size distribution (including average grain size G_{avg} and the standard deviation Σ of the grain size (Fig. 9(b, f, j), Fig. 10(b, f, j)), it is quantitatively demonstrated that two-step sintering (especially the sieved-powder derived samples) produces finer and more uniform microstructure than normal sintering. Specifically, the sieved-powder derived W-10Re sample two-step sintered at T_1=1200 °C for 0 h and T_2=1150 °C for 10 h gives G_{avg}=270 nm and Σ=103 nm (Fig. 9(b)), corresponding to a standard deviation $\sigma=\Sigma/G_{avg}$=0.38 of the normalized grain size G/G_{avg}), and the sieved-powder derived Mo sample two-step sintered at T_1=1120 °C for 0.5 h and T_2=1070 °C for 10 h gives G_{avg}=306 nm and Σ=110 nm (Fig. 10(b), corresponding to a standard deviation σ=0.36). They are among the best sintering practices in the respective material systems and the microstructural uniformity in terms of σ is also very good among all sintered materials [2]. The distributions of grain boundary misorientation angles are similar in all the samples (Fig. 9(c, g, k), Fig. 10(c, g, k)) and they all agree well with Mackenzie's theoretical distribution [56] for the randomly oriented cubic grains shown by dash lines. It

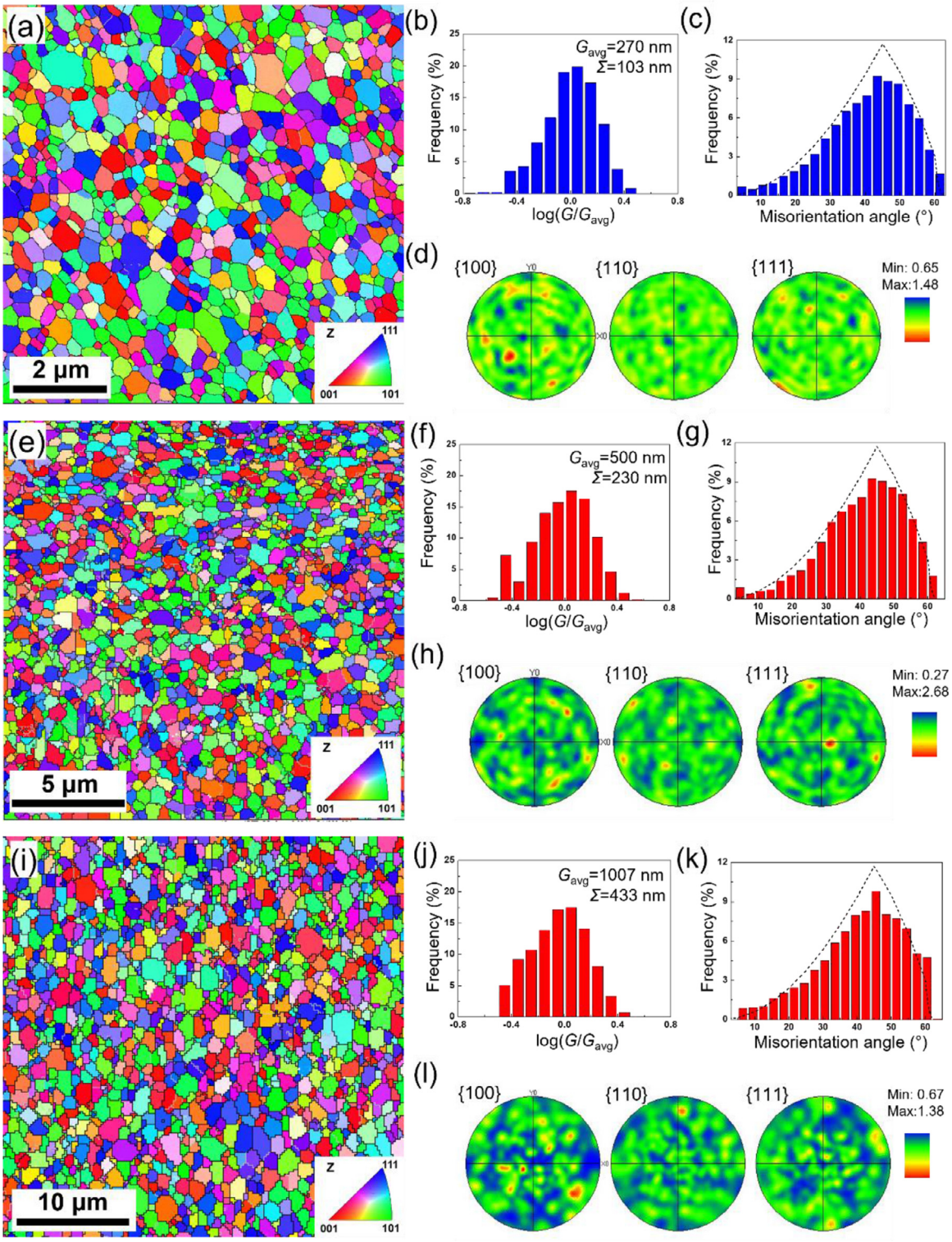

Fig. 9. EBSD results of (a-d) the sieved-powder derived W-10Re sample two-step sintered at T_1=1200 °C for 0 h and T_2=1150 °C for 10 h, (e-h) the raw-powder derived W-10Re sample two-step sintered at T_1=1300 °C for 0 h and T_2=1200 °C for 10 h, and (i-l) the raw-powder derived W-10Re sample sintered at 1500 °C for 0 h. (a, e, i) Inverse pole figure map, (b, f, j) normalized grain size distribution, (c, g, k) distributions of grain boundary misorientation angles (dash lines: Mackenzie's distribution for randomly oriented cubic grains [56]), and (d, h, l) pore figures.

suggests the absence of preferred grain orientations and relatively isotropic polycrystal packing. The isotropic polycrystal packing is further supported by the pole figures (Fig. 9(d, h, l), Fig. 10(d, h, l)), which do not have any obvious textures, though the texture signals are even weaker in two-step sintered samples.

3.6. Vickers hardness and its Weibull modulus

The finer and more uniform microstructure produced by two-step sintering should translate to better mechanical properties, and we demonstrate this by indentation tests. We expect higher aver-

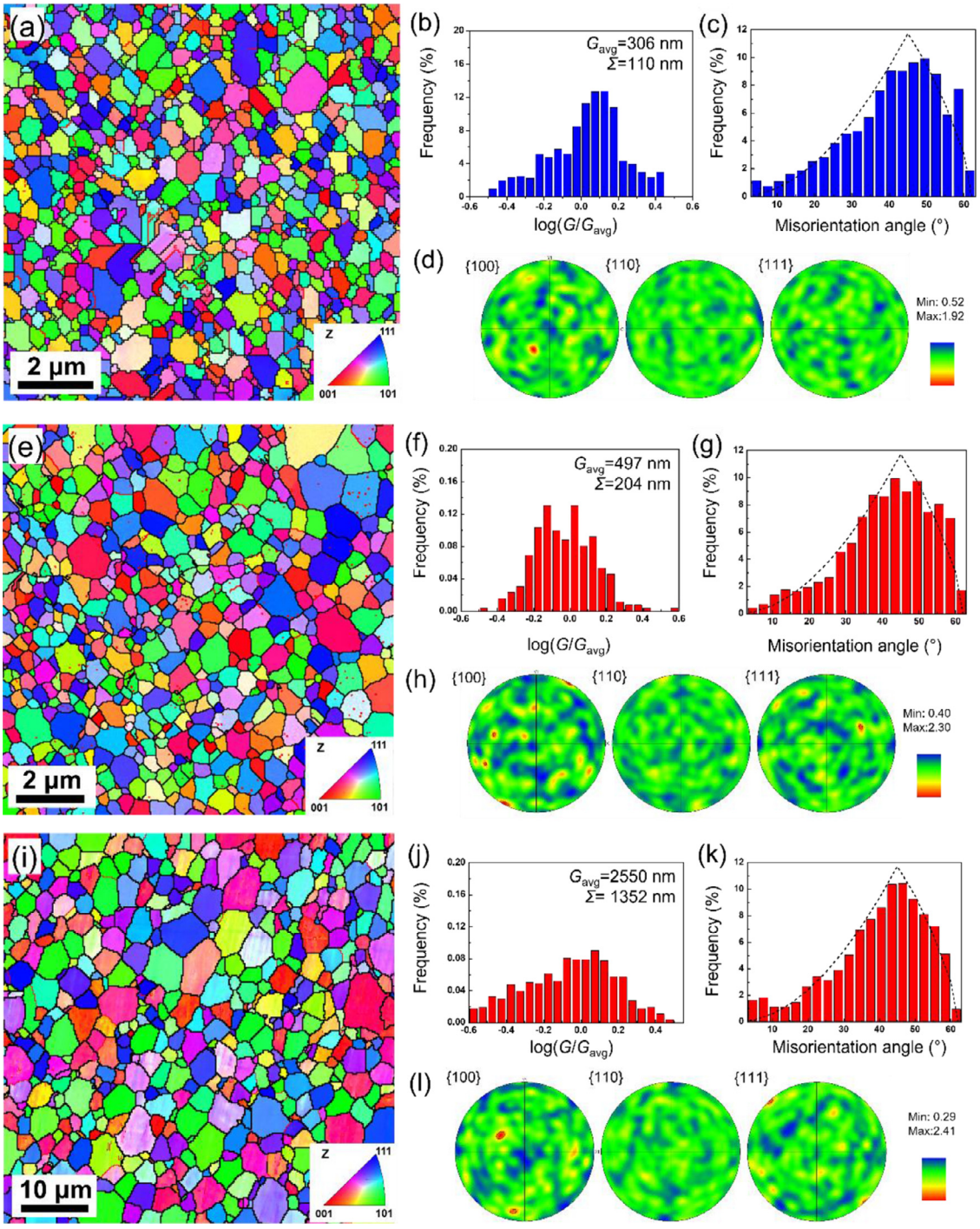

Fig. 10. EBSD results of (a-d) the sieved-powder derived Mo sample two-step sintered at T_1=1120 °C for 0.5 h and T_2=1070 °C for 10 h, (e-h) the raw-powder derived Mo sample two-step sintered at T_1=1120 °C for 0.5 h and T_2=1070 °C for 10 h, and (i-l) the raw-powder derived Mo sample sintered at 1300 °C for 0.5 h. (a, e, i) Inverse pole figure map, (b, f, j) normalized grain size distribution, (c, g, k) distributions of grain boundary misorientation angles (dash lines: Mackenzie's distribution for randomly oriented cubic grains [56]), and (d, h, l) pore figures.

age hardness H_{avg} from finer grain size and larger Weibull modulus m of the hardness (i.e., less scattered hardness data) from improved microstructural uniformity. For W-10Re (Fig. 11(a)), we compared the sieved-powder derived sample two-step sintered at T_1=1200 °C for 0 h and T_2=1150 °C for 10 h (abbreviated as "sieved W-10Re, TSS"), the raw-powder derived sample two-step sintered at T_1=1300 °C for 0 h and T_2=1200 °C for 10 h (abbreviated as "raw W-10Re, TSS"), and the raw-powder derived sample sintered at 1500 °C for 0 h (abbreviated as "raw W-10Re, NS"). Among them, sieved W-10Re, TSS shows the highest H_{avg}=6.3 GPa and largest m=25. We also compared our data with hardness data of W-Re alloys in the literature (Fig. 11(b)), where our data lie on the corner of finer grain size and higher hardness. The data also follow a Hall-Petch type relationship, which indicates good grain boundary cohesion without softening. For Mo (Fig. 12(a)), we compared the sieved-powder derived Mo sample two-step sintered at T_1=1120 °C for 0.5 h and T_2=1070 °C for 10 h (abbreviated as "sieved Mo, TSS"), the raw-powder derived Mo sample two-step sintered at T_1=1120 °C for 0.5 h and T_2=1070 °C for 10 h (abbreviated as "raw Mo, TSS"), and the raw-powder derived Mo sam-

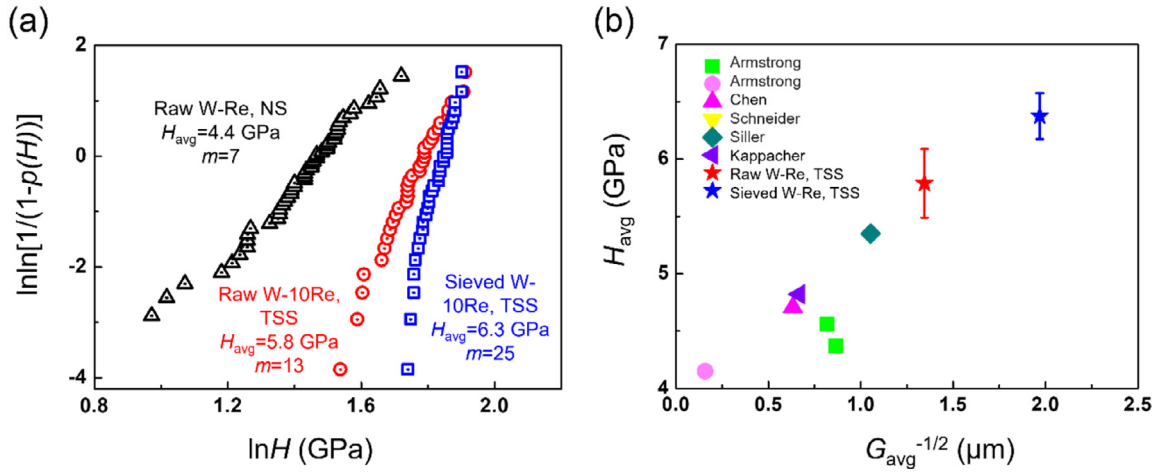

Fig. 11. (a) Weibull distribution of Vickers hardness for the sieved-powder derived W-10Re sample two-step sintered at T_1=1200 °C for 0 h and T_2=1150 °C for 10 h (abbreviated as "sieved W-10 Re, TSS" in blue), the raw-powder derived W-10Re sample two-step sintered at T_1=1300 °C for 0 h and T_2=1200 °C for 10 h (abbreviated as "raw W-10Re, TSS" in red), and the raw-powder derived W-10Re sample sintered at 1500 °C for 0 h (abbreviated as "raw W-10Re, NS" in black). (b) Comparison of our hardness data with the literature reports [25,57-61].

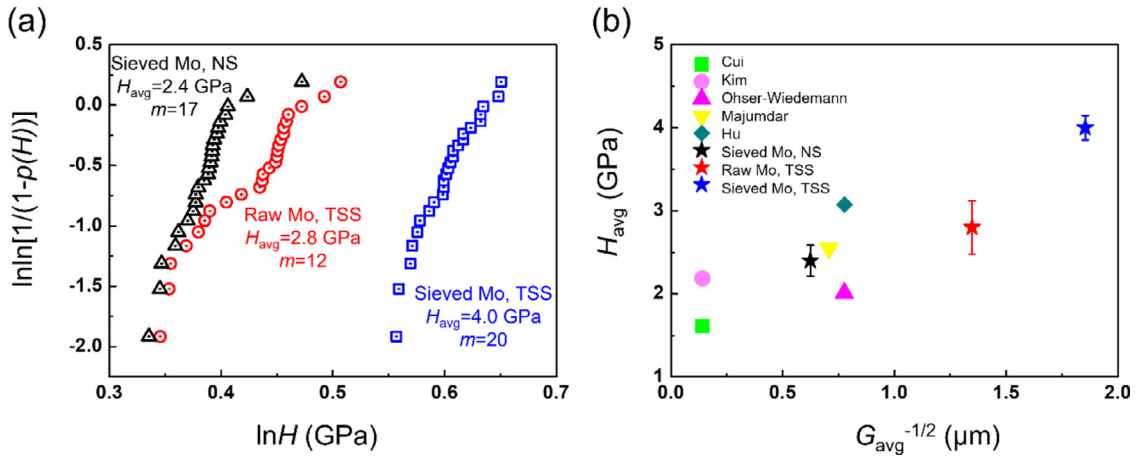

Fig. 12. (a) Weibull distribution of Vickers hardness for the sieved-powder derived Mo sample two-step sintered at T_1=1120 °C for 0.5 h and T_2=1070 °C for 10 h (abbreviated as "sieved Mo, TSS" in blue), the raw-powder derived Mo sample two-step sintered at T_1=1120 °C for 0.5 h and T_2=1070 °C for 10 h (abbreviated as "raw Mo, TSS" in red), and the raw-powder derived Mo sample sintered at 1300 °C for 0.5 h (abbreviated as "raw Mo, NS" in black). (b) Comparison of our hardness data with the literature reports [30,32,33,45,62].

ple sintered at 1300 °C for 0.5 h (abbreviated as "raw Mo, NS"). Among them, sieved Mo, TSS shows the highest H_{avg}=4.0 GPa and the largest m=20. Compared with literature data (Fig. 12(b)), our data in Mo again show finer grain size and higher hardness, though the Hall-Petch trend is noisier. These results confirm the microstructure-properties correlation and prove two-step sintering as an effective method to produce better refractory metals/alloys.

4. Discussion

In the above, we successfully applied two-step sintering to W-10Re and Mo. Started with ~50 nm nano powders, dense W-10Re and Mo can be produced with ~300 nm final grain size. This corresponds to 6-fold coarsening from starting powders to sintered pellets, which is comparable to 6-fold coarsening in W and 6 to 10-fold coarsening in Al_2O_3, and larger than 2-fold coarsening in $BaTiO_3$-based ceramics [2]. A noticeable difference between metallic and ceramic systems lies in the sintering step when the coarsening takes place: In the optimized two-step sintering of ceramics, coarsening only takes place in the first sintering step at T_1 and can be completely frozen in the second sintering step at T_2; in contrast, for W, W-10Re, and Mo, coarsening takes place at both steps and we observed ~3-fold coarsening in the first sintering step at T_1 and another ~2-fold in the second sintering step at T_2 for optimized two-step sintering. We explained this by smaller Burgers vectors in metallic systems than ceramics, which makes shear-coupled grain boundary migration easier at low homologous temperatures. But this could be also due to the high-purity metallic samples, which experience less impurity segregation and drag at grain boundaries thus have more intrinsic grain boundary characteristics such as high mobility. Comparing W, W-10Re, and Mo, we found that the critical density ρ_c to start the second sintering step increases from ~71% in W to ~78% in W-10Re to ~81% in Mo (all for the sieved-powder derived samples, and all powders were synthesized and processed in the same way). Because ρ_c is closely related to the distribution of the dihedral angles between grain boundaries and surfaces and the critical grain-to-pore size ratio, it suggests that the anisotropy in interfacial energies follows the rank of Mo>W-10Re>W. (Therefore, the more uniform microstructure observed in partially sintered W-10Re than W in Section 2.2 should come from better powder characteristics.) These ρ_c data span from those of cubic ceramics (~73% in $BaTiO_3$ [52],

~75% in Y_2O_3 [50,51], 76% in $Ni_{0.2}Cu_{0.2}Zn_{0.6}Fe_2O_4$ [51]) to that of hexagonal Al_2O_3 (~83% [53,54]). Lastly, we note that the first- and second-step sintering temperatures of the best W, W-10Re, and Mo samples all lie within a narrow range (150 °C) from 1070 °C to 1230 °C (T_1=1230 °C for W, 1200 °C for W-10Re, and 1120 °C for Mo, and T_2=1180 °C for W, 1150 °C for W-10Re, and 1070 °C for Mo), despite 800 °C difference in their melting temperatures. We suspect that this may be related to some volatile impurities such as oxygen and nitrogen, which slows down sintering and can only be removed above certain temperatures.

5. Conclusions

(1) Pressureless two-step sintering of W-10Re and Mo has been demonstrated. The best sintering practices produce 98.4% dense W-10Re with an average grain size of 260 nm below 1200 °C and 98.3% dense Mo with an average grain size of 290 nm below 1120 °C.
(2) Centrifuge-sieving narrows down particle size distribution, improves sinterability of W-10Re and Mo nano powders, and results in better two-step sintering.
(3) Using sintering data, we found W-10Re and W have similar grain boundary diffusivity at the same homologous temperature and similar activation energy E_a of grain boundary diffusivity, while Mo has more sluggish grain boundary diffusivity and larger activation energy. From Johnson's method, E_a is 2.5 eV for W-Re and 4.3 eV for Mo, compared to 2.2 eV for W. From Herring's method, E_a is 2.9 eV for W-Re and 3.9 eV for Mo, compared to 3.5 eV for W. These values are smaller than the reported ones in the literature for the corresponding material systems, indicating good sinterability of the sieved nano powders.
(4) Two-step sintering is able to produce finer and more uniform microstructure than normal sintering by suppressing final-stage grain growth and microstructural bifurcation. This translates to improved mechanical properties and reliability, such as higher hardness and larger Weibull modulus.
(5) We expect pressureless two-step sintering to be a general method to produce dense ultrafine-grained refractory metals and alloys. The key lies at proper powder processing and optimized sintering schedule. Further grain size refinement to nanocrystallinity requires finer and de-agglomerated nano powders, better compacting techniques for green bodies (high-pressure cold isostatic press, or warm press), and the addition of second-phase particles (e.g., dispersed oxide and carbide nanoparticles) to pin grain boundary motion.

Acknowledgments

Que, Z. Wei, X. Li, L. Zhang, M. Qin, and X. Qu acknowledge the financial supports by the Natural Science Foundation of China (52074032, 51974029, 52131307, 52071013) and "111" Project (No. B170003). Y.D. and J.L. acknowledge the support by Eni S.p.A. through the MIT Energy Initiative.

Supplementary materials

Supplementary material associated with this article can be found, in the online version, at doi:10.1016/j.jmst.2022.01.033.

References

[1] Z.Z. Fang, H. Wang, V. Kumar, Int. J. Refract. Met. Hard Mater. 62 (2017) 110–117.
[2] Y. Dong, H. Yang, L. Zhang, X. Li, D. Ding, X. Wang, J. Li, J. Li, I.W. Chen, Adv. Funct. Mater. 31 (2021) 1–9.
[3] X. Li, L. Zhang, Y. Dong, R. Gao, M. Qin, X. Qu, J. Li, Acta Mater 186 (2020) 116–123.
[4] X. Li, L. Zhang, Y. Dong, M. Qin, Z. Wei, Z. Que, J. Yang, X. Qu, J. Li, Acta Mater 220 (2021).
[5] A. Hasegawa, M. Fukuda, K. Yabuuchi, S. Nogami, J. Nucl. Mater. 471 (2016) 175–183.
[6] S. Wurster, B. Gludovatz, R. Pippan, Int. J. Refract. Met. Hard Mater. 28 (2010) 692–697.
[7] T. Tanabe, C. Eamchotchawalit, C. Busabok, S. Taweethavorn, M. Fujitsuka, T. Shikama, Mater. Lett. 57 (2003) 2950–2953.
[8] A. Taran, D. Voronovich, S. Plankovskyy, V. Paderno, V. Filipov, Electron. Dev. 56 (2009) 812–817.
[9] D. Scheiber, R. Pippan, P. Puschnig, A. Ruban, L. Romaner, Int. J. Refract. Met. Hard Mater. 60 (2016) 75–81.
[10] B.V. Petukhov, Crystallogr. Rep. 52 (2007) 112–122.
[11] W. Setyawan, R.J. Kurtz, Scr. Mater. 66 (2012) 558–561.
[12] R. Kirchheim, Scr. Mater. 67 (2012) 767–770.
[13] M. Stoica, J. Eckert, S. Roth, A.R. Yavari, L. Schultz, Ø. Rod, (2006) 11–13.
[14] E. Oda, K. Ameyama, S. Yamaguchi, Mater. Sci. Forum 503–504 (2006) 573–578.
[15] C. Ren, Z.Z. Fang, M. Koopman, B. Butler, J. Paramore, S. Middlemas, Int. J. Refract. Met. Hard Mater. 75 (2018) 170–183.
[16] W. Hu, Z. Dong, L. Yu, Z. Ma, Y. Liu, J. Mater. Sci. Technol. 36 (2020) 84–90.
[17] Z. Dong, N. Liu, W. Hu, Z. Ma, C. Li, C. Liu, Q. Guo, Y. Liu, J. Mater. Sci. Technol. 36 (2020) 118–127.
[18] Q. Zhou, J. Zhao, J.Y. Xie, F. Wang, P. Huang, T.J. Lu, K.W. Xu, Mater. Sci. Eng. A 608 (2014) 184–189.
[19] L.J. Kecskes, K.C. Cho, R.J. Dowding, B.E. Schuster, R.Z. Valiev, Q. Wei, Mater. Sci. Eng. A 467 (2007) 33–43.
[20] Z. Chen, M. Qin, J. Yang, L. Zhang, B. Jia, X. Qu, J. Mater. Sci. Technol. 58 (2020) 24–33.
[21] E.R. Onainor, Ninla Elmawati Falabiba 1 (2019) 12–47.
[22] N. na Qiu, Y. Zhang, C. Zhang, H. Tong, X.P. Song, Int. J. Miner. Metall. Mater. 25 (2018) 1055–1059.
[23] S. Pramanik, A.K. Srivastav, B. Manuel Jolly, N. Chawake, B.S. Murty, Adv. Powder Technol. 30 (2019) 2779–2786.
[24] E.Y. Ivanov, C. Suryanarayana, B.D. Bryskin, Mater. Sci. Eng. A 251 (1998) 255–261.
[25] C. Lai, J. Wang, F. Zhou, W. Liu, N. Miao, J. Alloys Compd. 735 (2018) 2685–2693.
[26] G. Liu, G.J. Zhang, F. Jiang, X.D. Ding, Y.J. Sun, J. Sun, E. Ma, Nat. Mater. 12 (2013) 344–350.
[27] G.S. Kim, Y.J. Lee, D.G. Kim, Y. Do Kim, J. Alloys Compd. 454 (2008) 327–330.
[28] W. Hu, T. Sun, C. Liu, L. Yu, T. Ahamad, Z. Ma, J. Mater. Sci. Technol. 88 (2021) 36–44.
[29] T. Takida, H. Kurishita, M. Mabuchi, T. Igarashi, Y. Doi, T. Nagae, Mater. Trans. 45 (2004) 143–148.
[30] C. Cui, Y. Gao, S. Wei, G. Zhang, Y. Zhou, X. Zhu, S. Guo, Appl. Phys. A: Mater. Sci. Process. 122 (2016) 214.
[31] J.L. Johnson, Sinter. Adv. Mater. (2010) 356–388.
[32] G.S. Kim, H.G. Kim, D.G. Kim, S.T. Oh, M.J. Suk, Y. Do Kim, J. Alloys Compd. 469 (2009) 401–405.
[33] P. Hu, T. Chen, X. Li, J. Gao, S. Chen, W. Zhou, J. Wang, Int. J. Refract. Met. Hard Mater. 83 (2019).
[34] M. Qin, Z. Chen, P. Chen, S. Zhao, R. Li, J. Ma, X. Qu, Int. J. Refract. Met. Hard Mater. 68 (2017) 145–150.
[35] S. Gu, M. Qin, H. Zhang, J. Ma, X. Qu, Int. J. Refract. Met. Hard Mater. 76 (2018) 90–98.
[36] C. Compounds, Choice Rev. Online. 37 (2000) 37–2788.
[37] K.L. Jiao, L.H. Chang, R. Wallace, W.A. Anderson, Appl. Supercond. 3 (1995) 55–60.
[38] T.S. Srivatsan, B.G. Ravi, M. Petraroli, T.S. Sudarshan, Int. J. Refract. Met. Hard Mater. 20 (2002) 181–186.
[39] M. Broniatowski, J. Stat. Plan. Inference. 35 (1993) 349–365.
[40] D.L. Johnson, J. Appl. Phys. 40 (1969) 192–200.
[41] W.S. YOUNG, I.B. CUTLER, J. Am. Ceram. Soc. 53 (1970) 659–663.
[42] D. Scheiber, R. Pippan, P. Puschnig, L. Romaner, Model. Simul. Mater. Sci. Eng. 24 (2016) 085009.
[43] C. Herring, J. Appl. Phys. 301 (1950) 4–7.
[44] J.D. Hansen, R.P. Rusin, M. Teng, D.L. Johnson, J. Am. Ceram. Soc. 75 (1992) 1129–1135.
[45] S. Majumdar, S. Raveendra, I. Samajdar, P. Bhargava, I.G. Sharma, Acta Mater 57 (2009) 4158–4168.
[46] N.C. Kothari, J. Less-Common Met. 5 (1963) 140–150.
[47] R.M. German, Z.A. Munir, Metall. Trans. A 7 (1976) 1873–1877.
[48] A.K. Srivastav, M. Sankaranarayana, B.S. Murty, Metall. Mater. Trans. A 42 (2011) 3863–3866.
[49] T. Vasilos, J.T. Smith, J. Appl. Phys. 35 (1964) 215–217.
[50] I.W. Chen, X.H. Wang, Nature 404 (2000) 168–171.
[51] X.H. Wang, P.L. Chen, I.W. Chen, J. Am. Ceram. Soc. 89 (2006) 431–437.
[52] X.H. Wang, X.Y. Deng, H.L. Bai, H. Zhou, W.G. Qu, L.T. Li, I.W. Chen, J. Am. Ceram. Soc. 89 (2006) 438–443.
[53] H. Yang, L. Li, Y. Li, B. Shen, Y. Kang, L. Zhao, J. Li, Y. Dong, J. Li, J. Materiomics 7 (2021) 837–844.
[54] H. Yang, L. Li, W. Cao, Y. Liu, M. Mukhtar, L. Zhao, Y. Kang, Y. Dong, J. Li, J. Eur. Ceram. Soc. 40 (2020) 1505–1512.
[55] Y. Dong, I.W. Chen, J. Am. Ceram. Soc. 101 (2018) 1857–1869.
[56] J.K. Mackenzie, M.J. Thomson, Biometrika 44 (1957) 205.
[57] D.E.J. Armstrong, T.B. Britton, Mater. Sci. Eng. A 611 (2014) 388–393.

[58] D.E.J. Armstrong, X. Yi, E.A. Marquis, S.G. Roberts, J. Nucl. Mater. 432 (2013) 428–436.
[59] J. Schneider, J. Terrell, L. Farris, D. Tucker, T. Leonhardt, H. Goldbeck, Metall. Mater. Trans. B 51 (2020) 35–44.
[60] M. Siller, J. Schatte, S. Gerzoskovitz, W. Knabl, R. Pippan, H. Clemens, V. Maier-Kiener, Int. J. Refract. Met. Hard Mater. 92 (2020) 105285.
[61] J. Kappacher, A. Leitner, D. Kiener, H. Clemens, V. Maier-Kiener, Mater. Des. 189 (2020) 108499.
[62] Y. Kim, S. Lee, J.W. Noh, S.H. Lee, I.D. Jeong, S.J. Park, Int. J. Refract. Met. Hard Mater. 41 (2013) 442–448.